Highly Mobile Excitons in Single Crystal Methylammonium Lead Tribromide Perovskite Microribbons

Luke McClintock,[†] Ziyi Song,[†] H. Clark Travaglini,[†] R. Tugrul Senger,^{‡,¶}
Vigneshwaran Chandrasekaran,[§] Han Htoon,[§] Dmitry Yarotski,[§] and Dong Yu[†]
†Department of Physics, University of California-Davis, One Shields Avenue, Davis, CA
95616

‡Department of Physics, Izmir Institute of Technology, 35430 Izmir, Turkey

¶ICTP-ECAR Eurasian Center for Advanced Research, Izmir Institute of Technology,

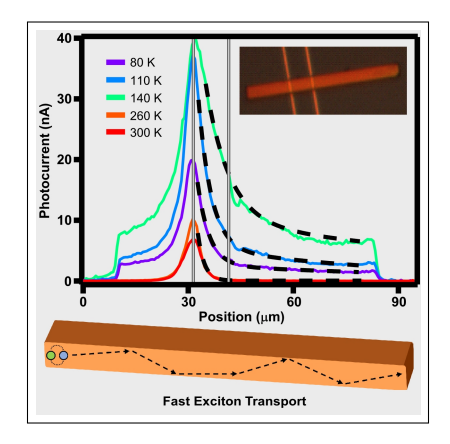
35430 Izmir, Turkey

§ Center for Integrated Nanotechnology, Los Alamos National Laboratory, Los Alamos, NM, 87545

Abstract

Excitons are often given negative connotation in solar energy harvesting in part due to their presumed short diffusion lengths. We investigate exciton transport in single-crystal methylammonium lead tribromide (MAPbBr₃) microribbons via spectrally, spatially, and temporally resolved photocurrent and photoluminescence measurements. Distinct peaks in the photocurrent spectra unambiguously confirm exciton formation and allow for accurate extraction of the low temperature exciton binding energy (39 meV). Photocurrent decays within a few μ m at room temperature, while a gate-tunable long-range photocurrent component appears at lower temperatures (about 100 μ m below 140 K). Carrier lifetimes of 1.2 μ s or shorter exclude the possibility of the long decay length arising from slow trapped-carrier hopping. Free carrier diffusion is also an unlikely source of the highly nonlocal photocurrent, due to their small fraction at low temperatures. We attribute the long-distance transport to high-mobility excitons, which may open up new opportunities for novel exciton-based photovoltaic applications.

TOC Graphic



Excitons, electron-hole pairs bound by Coulomb attraction, have major impacts on the optoelectronic properties and applications of semiconductor materials. In polymer semiconductors, excitons dominate over free charge carriers upon photoexcitation. Consequently, one of the limiting factors for power conversion efficiency in organic solar cells is the exciton diffusion length (L_D) , which is rather short, on the order of 10 nm. 2L_D is determined by the diffusivity D and the lifetime τ of the charge carriers $(L_D = \sqrt{D\tau})$, while D is related to the carrier mobility by $\mu = qD/k_BT$, as Einstein's relation is assumed for diffusive transport. In this case, the formation of excitons, their short diffusion lengths, as well as the difficulty of their separation into free charge carriers have posed significant challenges facing the applications of these materials in photovoltaics. However, excitons can also become highly mobile if electric screening is sufficient to suppress the phonon coupling, with mobility reaching as high as $10^6 \text{ cm}^2/\text{Vs}$ in silicon. 3

Excitons can form in hybrid halide perovskites in significant populations when the exciton binding energy (E_B) is comparable with, or larger than, the thermal energy (k_BT) . Exciton diffusion lengths in nanocrystals and two-dimensional (2D) layered perovskites range from 200 nm to 1 μ m ⁴⁻⁶ and excitons can lose mobility when significantly dressed by phonons in one-dimensional (1D) perovskites.⁷ The limits of exciton mobility and diffusion length in single crystals of three-dimensional (3D) perovskites are unclear. Understanding the intrinsic exciton transport properties in 3D single crystals provides a solid basis to compare with their low-dimensional and nanocrystal counterparts. Recently, we have observed that carrier diffusion length increases rapidly as temperature decreases in single-crystal methylammonium lead triiodide (MAPbI₃) microstructures, which can be understood by the exponentially growing fraction of highly mobile, free excitons at low temperature.^{8,9} Methylammonium lead tribromide (MAPbBr₃) has a larger E_B than MAPbI₃ and hence provides a convenient platform to study excitons. Here, we investigate temperature-dependent dynamics and transport of coexisting photogenerated excitons and free carriers in MAPbBr₃ single crystal microribbon field effect transistors (FETs), by using energetically, spatially, and temporally

resolved optical and optoelectronic techniques. By studying single crystal structures with nano/micro-scale thickness, we eliminate the complications caused by grain boundaries while also enabling in-situ gate tuning of the Fermi level. ¹⁰ In order to directly obtain exciton or carrier diffusion length, we use scanning photocurrent microscopy (SPCM), a powerful experimental technique that provides spatially resolved photocurrent mapping and insights on carrier transport. ^{11–14}

Single crystalline microstructures of MAPbBr₃ are synthesized following a dissolution and recrystallization process. ¹⁵ Structures with thickness ranging from 300 nm to 2 μ m and length up to 200 μ m are produced with well defined facets and smooth surfaces (Figure 1a,b). To avoid exposure of the sample to detrimental solvent processing, the as-grown crystals are directly transferred via micro-fiber to pre-patterned Cr/Au electrodes on SiO₂ coated Si substrates to fabricate FETs. The devices are quite insulating in the dark but become conductive under light. The nonlinear current-voltage relation (Figure S1 in the Supporting Information) indicates large contact barriers.

Temperature dependent photocurrent spectra are measured with a defocused laser, so that the entire microribbon is uniformly photoexcited. As temperature is reduced, a distinct peak is developed, indicating the exciton resonance (Figure 1c). The exciton peak position first redshifts when the temperature is reduced, but then abruptly blueshifts at 140 K (Figure 1d), corresponding to the tetragonal-orthorhombic phase transition. It then continues to redshift below 140 K. This trend is similar to previous reports ^{16–18} and is observed in our PL spectra measurements (shown later). The excitonic peak width narrows from 80 to 40 meV as the temperature is reduced from 260 K to 170 K and then stays around the same level except for a spike at the 140 K phase change (Figure 1e). The peak width at low temperature is larger than the value expected from phonon broadening, ¹⁹ indicating sample inhomogeneity due to the relatively large surface to volume ratio and the large laser spot size. We perform Elliott fittings (Equation S1 in the Supporting Information), convolved with Gaussian functions to account for thermal broadening, on the photocurrent spectra to

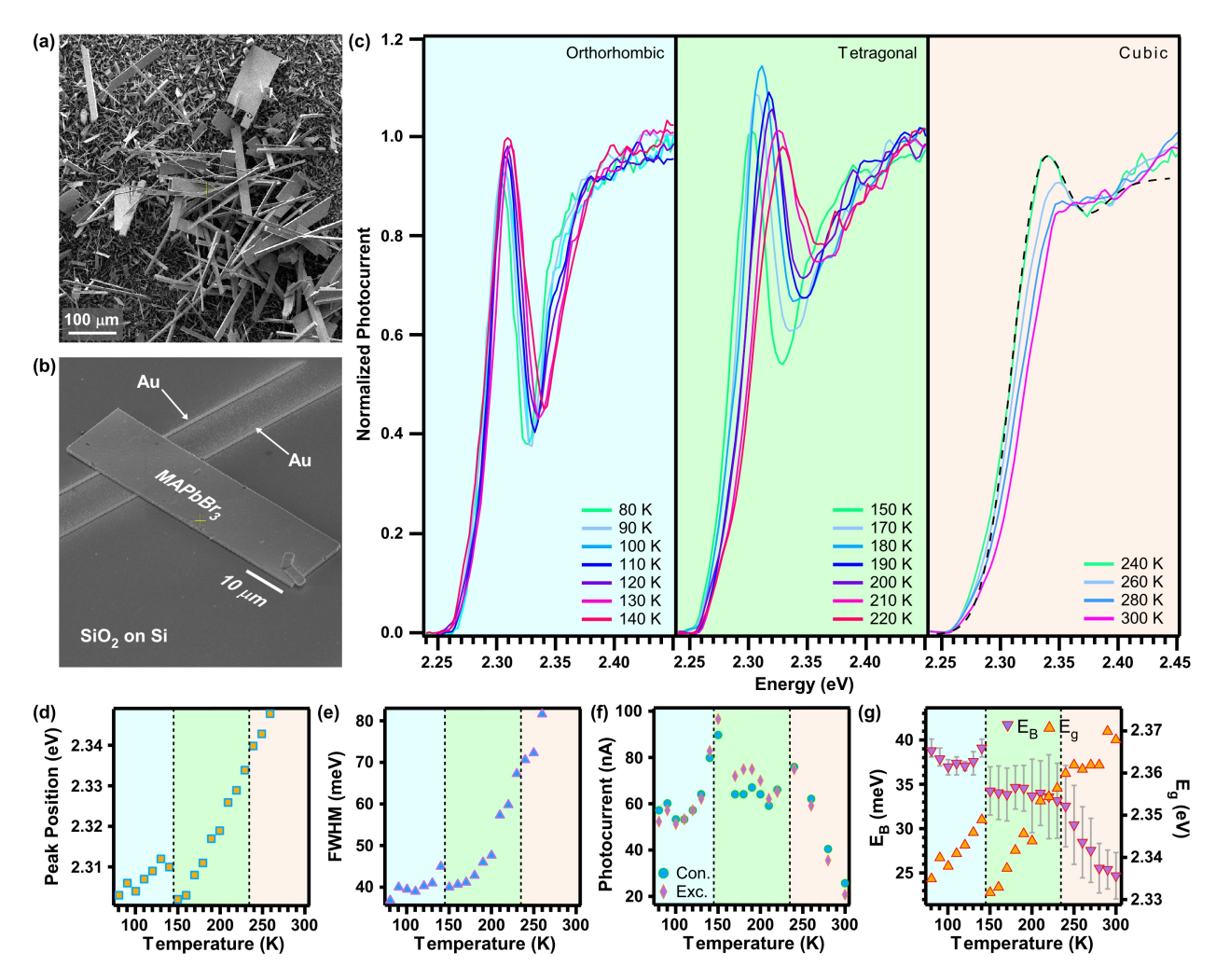


Figure 1: Temperature dependent photocurrent spectra and Elliott fittings of a typical MAPbBr₃ microribbon device. (a) SEM image of the as-grown samples on a substrate. (b) SEM image of a device, showing the MAPbBr₃ microribbon connected to bottom Au contacts. The microribbon length is 74 μ m and thickness is 640 nm. (c) Photocurrent spectra at various temperatures. Photocurrent is normalized at 2.45 eV. The laser power is about 5 μ W and defocused to an area of about 4000 μ m². $V_{SD} = 2$ V is applied. The dashed, black line represents an Elliott fitting example. (d) and (e) Excitonic peak position and full width at half maximum (FWHM) as functions of temperature, respectively. (f) Temperature dependent photocurrent values taken from 2.45 eV (Con.) and the excitonic peak (Exc.), respectively. (g) Exciton binding energy and bandgap energy as a function of temperature, extracted from (c) via the Elliott formula.

extract E_B and bandgap energy $(E_g)^{18,20-26}$ (Figure 1c,g, Figure S2, see details in Supporting Information). E_B grows steadily until the first phase change, where it then stagnates around 34 meV. It then abruptly jumps to about 39 meV at the second phase change, simultaneous with a sharp blueshift in E_g .

We next perform SPCM at various temperatures. A focused laser with a spot size of about 1 μ m is raster scanned while photocurrent is mapped as a function of laser position. A source-drain bias (V_{SD}) is applied to improve the photocurrent signal. The photocurrent cross sections along the microribbon axis are shown in Figure 2a. At 300 K and 260 K, photocurrent is only observed when the laser is close to the reversely biased contact, with a decay length of 2 - 3 μ m. Photocurrent appears both inside and outside the source-drain channel. The photocurrent generated by photoexcitation in the electric-field-free region outside the channel is caused by the diffusion of the photogenerated carriers. Below 220 K, the photocurrent profile looks slightly asymmetric with a longer decay length in the channel (most clear at 140 K). This is likely because the contact barrier is smaller at low temperature, creating a stronger in-channel electric field. Consequently, the carrier drift leads to enhanced photocurrent and longer L_D up to 7 μ m (Figure 2e) in channel.

Interestingly, a long tail with a smaller magnitude in the photocurrent distributions appears below 220 K (Figure 2a), in addition to the short decay component. A double-exponential fitting yields a decay length of $100 \pm 40 \mu m$ for the long-range component at low temperatures (Figure 2e). The large uncertainty arises from the microribbon's length, which is itself limited by the synthesis method. The photocurrent decay profiles are found to be insensitive to the excitation photon energy range used in the experiment (2.25-2.48 eV). The short decay length is comparable to the electron (minority carrier) diffusion length (1-5 μ m) reported in single crystal MAPbBr₃, ²⁷ but the long decay length is much larger than previously reported values. The long-range component's magnitude is peaked at 140 K and is about one quarter of the short component's magnitude (Figure 2d). A long-range photocurrent decay profile has also been observed in MAPbI₃ microribbons. However, the photocurrent behavior in MAPbBr₃ is drastically different from that in MAPbI₃. First, the photocurrent profile in MAPbI₃ follows well with a single exponential function, while MAPbBr₃ shows two distinct decay components. Second, the photocurrent decay length in MAPbI₃ reaches 200 μ m only at 80 K, while the decay length in MAPbBr₃ already increases

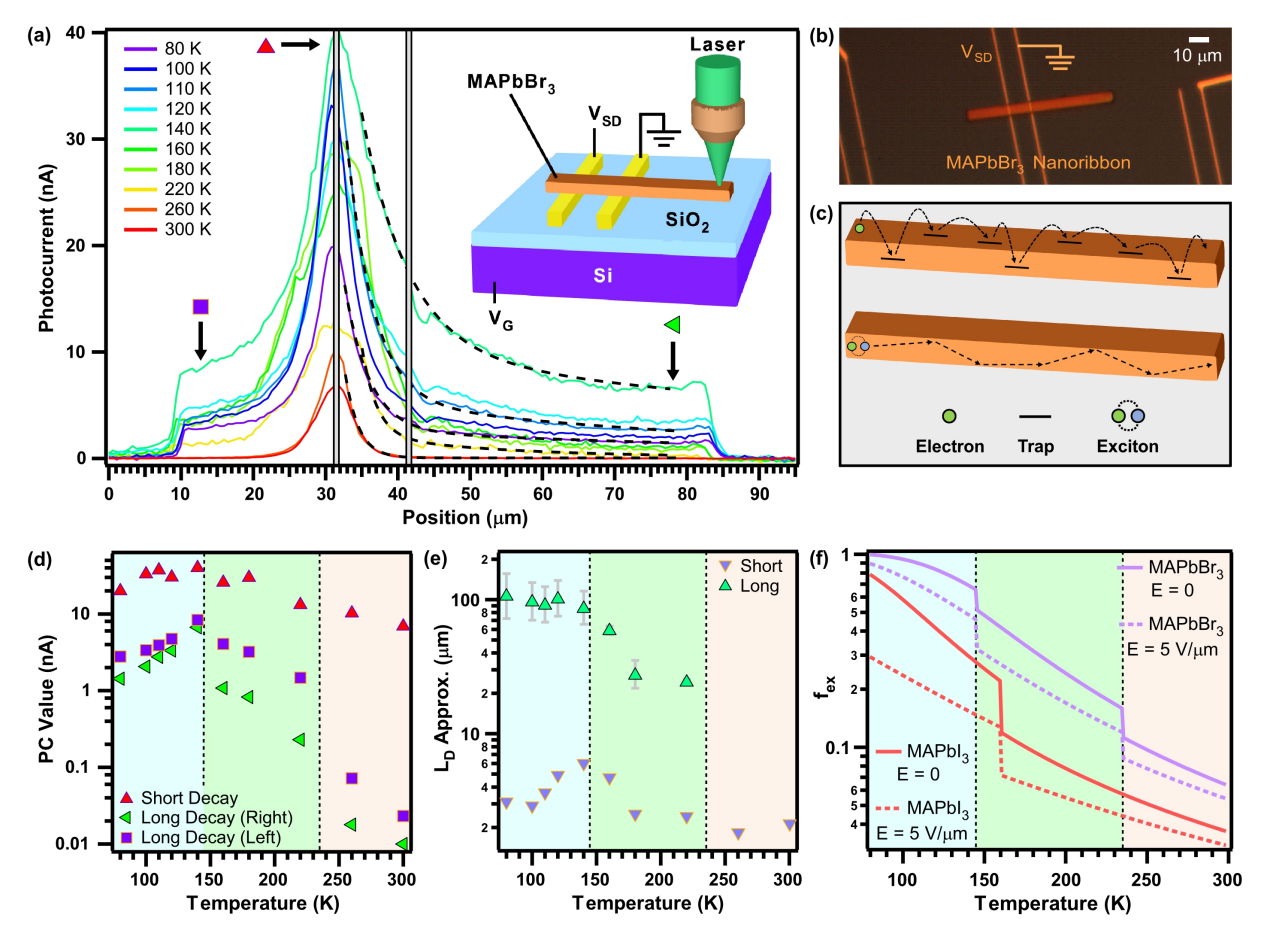


Figure 2: Spatially resolved photocurrent. (a) Photocurrent distributions along the microribbon axis at various temperatures. The laser power is 2 μ W at 510 nm. $V_{SD}=4$ V (5 V for 260 and 300 K) is applied across the channel. Dashed black lines represent double-exponential fittings of the photocurrent decays. Inset shows the SPCM schematic. (b) Optical image of a microribbon device. (c) Schematics for potential mechanisms, including trap hopping (top) and exciton transport (bottom). (d) Photocurrent magnitudes plotted against temperature, taken from SPCM profiles in (a), at three locations along the device (indicated with markers): at the contact (red triangles), at the right end (green triangles), and at the left end (purple squares). (e) L_D extracted from double-exponential curve fits in (a). There is no long-range component for 260 and 300 K. (f) Calculated exciton fraction as a function of temperature for MAPbI₃ and MAPbBr₃, in the field free region and the depletion region, respectively.

to 100 μ m around the orthorhombic phase transition temperature (140 K).

To understand the observed long decay length, we performed time-resolved PL (TRPL) at various temperatures. PL spectra exhibit a well defined peak at 11 K, which shifts to higher energy as temperature increases, consistent with the photocurrent spectra (Figure 3a,b). The FWHM is about 10 meV at 11 K and increases to 15 meV at 80 K (Figure 3c), significantly

narrower than the peak width measured in photocurrent spectra. Initially, the PL intensity decays rapidly, on a timescale of a few ns. This very fast decay can be attributed to Auger recombination ²² or surface recombination. ²⁸ As temperature decreases, a slower component of 10's of ns is observed (Figure 3d), and an even slower component of 100's of ns appears below 80 K. However, at the more relevant temperatures for our photocurrent studies, 80 K and above, this extra slow component is absent. These recombination lifetimes are also consistent with literature values. ^{28–30}

To examine the potentially slow nonradiative carrier recombination undetected by TRPL, we also perform time-resolved photocurrent (TRPC) by using a photoclastic modulator (PEM) based chopper (Figure S3). TRPC measurements yield a photocurrent decay time of $\sim 1.2 \ \mu s$, which is an upper bound of the real carrier lifetime because of the temporal resolution limitation of the instrument. Using the upper limit of the above determined lifetime of $\tau = 1.2 \ \mu s$ and a L_D value of 100 μm at 80 K, we extract a lower bound diffusion coefficient of $D = L_D^2/\tau \approx 83 \ cm^2/s$, which corresponds to an enormous mobility of $\mu = qD/k_BT \approx 10^4 \ cm^2/Vs$. Such a high carrier mobility is unlikely achieved by trapped charges hopping among traps (depicted in Figure 2c, top). In addition, the hopping mobility is usually suppressed at lower temperature and inconsistent with the longer L_D .

We now discuss the potential mechanisms that may account for the observed long-range photocurrent tails. Exciton-polaritons with a propagation distance of 60 μ m have been reported in CsPbBr₃ microcavity structures with distributed Bragg reflectors (DBR). Our microribbon devices are not embedded in such photonic structures and the observed 100 μ m photocurrent decay lengths do not require DBR. Without manufactured mirrors to confine the photons within the cavity, optical loss through PL emitted light escaping through the sample surfaces is expected, making it difficult to sustain such low-loss and long-distance polariton transport. Indeed, in MAPbBr₃ micro/nanowires without DBR, exciton-polaritons were only demonstrated in microwires shorter than 20 μ m. Therefore, exciton-polariton condensation is not a likely mechanism to account for the observed 100 μ m photocurrent

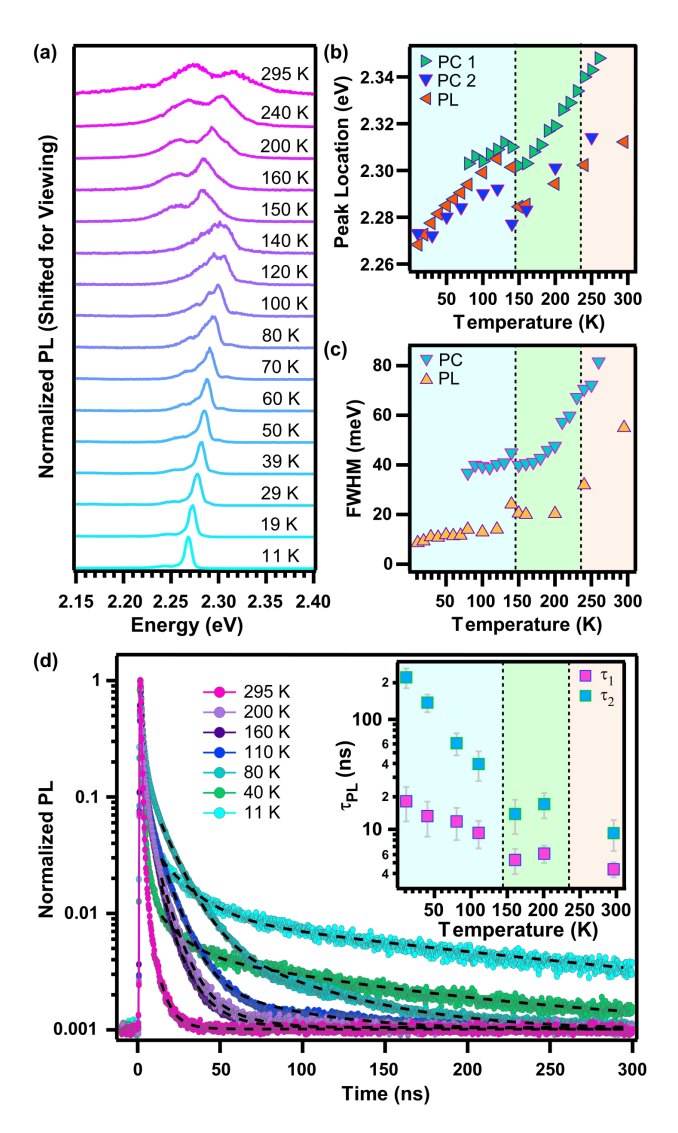


Figure 3: PL spectra and TRPL measurements under 405 nm excitation. (a) Normalized PL spectra across a wide range of temperatures, vertically shifted for better viewing. The average laser intensity varies from 3×10^{-2} to $1.6 \, \mathrm{W/cm^2}$ as the PL emission is much stronger at lower temperature. (b-c) Comparison of PL and photocurrent peak energy (b) and FWHM (c) as a function of temperature. PC values are extracted from Figure 1 and another device. (d) Normalized TRPL measurements as a function of temperature, with bi-exponential fittings used to extract carrier lifetimes. Average laser intensity varies from 0.3 to $14 \, \mathrm{W/cm^2}$ as temperature increases. Inset, extracted carrier lifetimes as a function of temperature.

decay lengths in our microribbons without manufactured cavities.

Free carrier diffusion also unlikely explains the observed highly non-local photocurrent in MAPbBr₃. Under photoexcitation, the excitons and free carriers quickly reach a dynamic balance through the fast pairing and dissociation process occurring on a picosecond timescale.³³ The fractions of the coexisting excitons and free carriers can be quantitatively estimated by the Saha-Langmuir equation.³⁴ At sufficiently low temperature $(k_BT \ll E_B)$, a majority of photoexcited charge carriers are bound into pairs. Using an exciton binding energy of 40 meV (as extracted from our photocurrent spectral data) and a hole concentration of 10^{16} cm⁻³ in the p-type material, we estimated from Saha's equation that photogeneration creates 99 % excitons and 1 % free carriers at 80 K (see details in the Supporting Information). This calculation is also supported by the very pronounced exciton peaks observed in our photocurrent and PL spectra at low temperatures. Furthermore, the diffusion length remains extremely long at 10 K (Figure S4b in Supporting Information), where E_B is 40 times larger than k_BT . Thus, it is highly unlikely that the observed long diffusion lengths originate from free carriers.

We attribute the strongly temperature dependent non-local photocurrent to efficient exciton transport. Similar to MAPbI₃, the excitons may have a much lower phonon scattering rate than free carriers. A calculation shows the exciton-LO phonon scattering rate is reduced by a factor of $\gamma = \left(\frac{18a_0^3 R_f}{4\epsilon_\infty R_x^4}\right)^2$, where a_0 is the the exciton Bohr radius, $R_e = \sqrt{\frac{\hbar}{2m_e\omega_{LO}}}$, $R_h = \sqrt{\frac{\hbar}{2m_h\omega_{LO}}}$, and $R_x = \sqrt{\frac{\hbar}{2m_x\omega_{LO}}}$ are the electron, hole, and exciton polaron radii, respectively, where m_e , m_h , and m_x are their corresponding effective masses, and ω_{LO} is the LO phonon frequency.⁸ Here, γ is estimated to be 5.3×10^{-4} in orthorhombic MAPbI₃ and 5.2×10^{-4} in orthorhombic MAPbBr₃ (parameters are shown in SI). The higher onset temperature for long L_D in MAPbBr₃ is consistent with its larger E_B . Though excitons are charge neutral, they can diffuse and split under the Schottky field at the contacts, leading to photocurrent. The photocurrent magnitude of the long-range tail first increases, caused by the increasing exciton fraction (f_{ex}) . Then it decreases below 140 K, likely because the lower thermal energy becomes less effective at dissociating excitons even when they enter the depletion region. We calculated f_{ex} from the Saha equation in the field-free region and in the depletion region by considering electric field effects (details shown in the Supporting Information). f_{ex} is significantly decreased under the electric field at the metal junction (estimated to be 5 V/ μ m) for MAPbI₃ but does not change much for MAPbBr₃ at 80 K (Figure 2f).

One significant difference with MAPbI₃ is that the MAPbBr₃ photocurrent distributions always exhibit a short decay component near the contact. MAPbBr₃ is known to have a higher defect density than MAPbI₃²⁸ and the defect density is expected to be significantly higher at the surface, causing a faster recombination. The short photocurrent decay near the contact may be due to the fast surface recombination. When the laser is far away from the contact, a large fraction of injected carriers recombine quickly at the surface. A smaller fraction of carriers (around 25% at 140 K), generated inside the microribbon away from surface, form excitons and travel with high mobility to the contact.

Finally, we briefly discuss the gate modulation on the non-local photocurrent. The application of a gate voltage (V_G) has negligible effect at room temperature, presumably due to ion migration in MAPbBr₃ which screens the gate induced electric field. At lower temperatures, however, V_G significantly modulates the conductivity of the MAPbBr₃ microribbon devices. The dark conductance drops by about an order of magnitude under positive V_G , indicating the device is p-type (Figure S6). The hole mobility extracted from the slope of the gate scan is $2.3 \times 10^{-3} \text{ cm}^2/\text{Vs}$. Note that this value is an underestimation of the actual hole mobility because of the large contact resistance. The gate scan also shows a bigger hysteresis at higher temperature, indicating ion migration or charge trapping. The photocurrent distributions are also sensitive to V_G in the MAPbBr₃ microribbon FET (Figure 4). The photocurrent inside the source-drain channel increases by a factor of 6 when V_G is increased to 50 V at $V_{SD}=1$ V, likely because the p-type channel becomes much more insulating and the voltage drop across the channel increases, leading to a larger photocurrent. At V_{SD} = 0.5 V, the non-local photocurrent can be completely turned on/off by gate (Figure 4b). This is likely because the weaker junction electric field is insufficient to split excitons in the absence of V_G . The non-local photocurrent outside the channel also increases at positive V_G . This can be attributed to the longer carrier recombination time as the positive V_G reduces the majority carrier (hole) concentration, though more work is needed to further clarify.

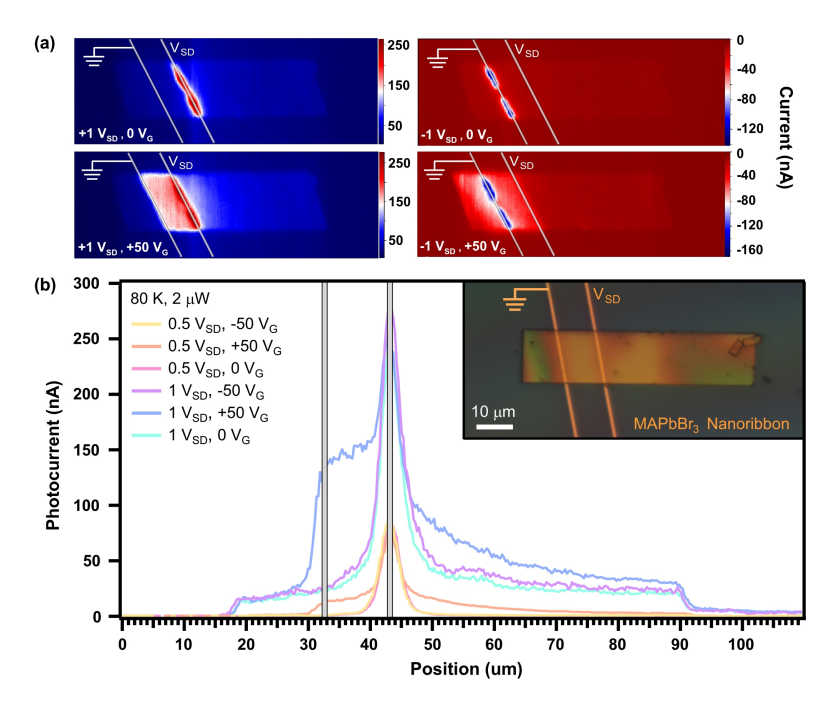


Figure 4: Gate dependent photocurrent profiles. (a) Gate dependent photocurrent maps at 80 K and $V_{SD} = 1$ and -1 V, respectively. White lines indicate electrode positions. (b) Biasand gate-dependent SPCM profiles along the long axis at 80 K. Inset, optical image of a MAPbBr₃ microribbon with bottom-contacts visible through the crystal due to MAPbBr₃'s partial transparency.

In summary, we have observed, via photocurrent mapping, gate-tunable exciton diffusion lengths up to 100 μ m below 140 K in single-crystal MAPbBr₃ microribbons. The onset temperature for observing this long decay length in MAPbBr₃ (140 K) is significantly higher than that in MAPbI₃ (80 K), consistent with the larger exciton binding energy in MAPbBr₃. Along with a carrier lifetime of 1.2 μ s or shorter determined from time-resolved measurements, we estimate a high exciton mobility on the order of 10⁴ cm²/Vs. The high mobility is most likely due to the dipolar nature of the excitons, as they interact with phonons much less than monopolar free carriers. Formation of exciton-polaritons unlikely explains the 100 μ m photocurrent decay length since our microribbons are not optically confined in a fabricated photonic cavity. This work offers key insights on fast exciton transport in halide perovskite systems. It also provides methods for electrical detection and manipulation of exciton transport. The observed long exciton diffusion lengths may motivate unique designs

of exciton-based photovoltaic materials and devices.

Methods

Nano- and microstructure growth and device fabrication. 6 mg of MABr powder (Sigma Aldrich >98%) was slowly dissolved in 1 mL of isopropyl alcohol (IPA 99.5%) in a glass vial inside a nitrogen glovebox. Meanwhile 100 mg of PbAc₂ 3H₂O (Sigma Aldrich 99.999%) powder was dissolved in 1 mL of deionized water. The lead acetate trihydrate solution was distributed across FTO-coated glass slides via manual spreading with a pipette while baking on a hot plate at 90 °C until dry and then placed upside down inside the vial of MABr solution at 40 °C for 1-3 days. Afterwards, the substrate was removed and gently dipped into IPA for a few seconds, and then blown dry with nitrogen. The as-grown structures were then mechanically transferred via a microfiber to 300 nm SiO₂ covered Si substrates with pre-patterned 5 nm Cr/ 35 nm Au electrodes, to achieve single micro- and microribbon FETs.

Optoelectronic measurements. All measurements were performed in an optical cryostat (Janis ST-500) with a pressure of 10^{-6} Torr. Current-voltage curves and photocurrent spectra were measured through a current preamplifier (DL Instruments, model 1211) and a NI data acquisition system. SPCM measurements were performed using a home-built setup based upon an Olympus microscope. A wavelength-tunable laser (NKT SuperK) was focused by a 40x objective lens to a diffraction limited spot about 1 μ m in diameter and raster scanned on a planar device by a pair of mirrors mounted on galvanometers to produce 2D photocurrent maps. The position value is converted from the voltage output to the scan mirror. The angle of the mirror (and hence the position of the laser) is proportional to this voltage. The conversion factor has been calibrated. For transient photocurrent measurements, we used a photoelastic modulator to modulate the light intensity at 50 kHz with a light intensity decay time of about 1 μ s (see more in Supporting Information).

Photoluminescence measurements. A picosecond pulsed laser (Picoquant LDH-D-C-405) with a wavelength of 405 nm and pulse width of 56 ps was used for excitation. The laser was reflected through a dichroic beamsplitter (Semrock Di02-R405) and then focused onto the sample to a diffraction limited spot size using a 50x, 0.7NA Olympus objective microscope (LCPLFLN50xLCD), which was used to both excite the sample and collect the PL. Collected photons after passing through the same dichroic beamsplitter and a 496 nm longpass filter either go to a spectrometer+CCD (Acton SP2300i, pylon100) or a single photon avalanche photodiode (Excelitas SPCM-AQRH-14). TRPL was analyzed using a TCSPC module (Picoquant Hydraharp 400). For spectra, a focusing lens was used before the objective to uniformly illuminate smaller samples with a spot size of about 30 μ m. Then the spectrometer slit was closed to the smallest width of 10 μ m to analyze the spectra in the region of interest. The average laser intensity varies from 0.3 W/cm² at low temperature to 14 W/cm² at room temperature, where the emission is much weaker (intensity dependence is discussed in the Supporting Information).

Supporting Information

Supporting Information Available: Current-voltage curves at various illumination intensities; details of Elliott fitting; calculation of temperature- and electric-field-dependent exciton fractions; calculated free carrier fraction at various temperatures and experimentally measured photocurrent profile at 10 K; a table of simulation parameters; transient photocurrent measurement for extracting carrier recombination lifetime; power dependence of transient photoluminescence and photocurrent.

AUTHOR INFORMATION

Corresponding Authors

*E-mail: yu@physics.ucdavis.edu.

ORCID

Dong Yu: 0000-0002-8386-065X

R. T. Senger: 0000-0003-0800-1924

Notes

The authors declare that they have no competing financial interests.

ACKNOWLEDGEMENTS

We thank Mykyta Dementyev, Eric Beery, and Bob Wang for assistance in device creation

and photocurrent measurements. This work was supported by the U.S. National Science

Foundation Grants DMR-1710737 and DMR-1838532. Part of this study was carried out

at the UC Davis Center for Nano and Micro Manufacturing (CNM2). Device fabrication

was partially carried out at the Molecular Foundry, which is funded by the Office of Sci-

ence, Office of Basic Energy Sciences, of the U.S. Department of Energy under Contract

No. DE-AC02-05CH11231. R.T.S. acknowledges the support from The Turkish Fulbright

Commission Visiting Scholar Program. L. M. acknowledges the DOE SCGSR fellowship and

UC-National lab in-residence graduate fellowship. The TRPL work was performed at the

Center for Integrated Nanotechnologies, an Office of Science User Facility operated for the

U.S. Department of Energy (DOE) Office of Science. Los Alamos National Laboratory, an

affirmative action equal opportunity employer, is managed by Triad National Security, LLC

for the U.S. Department of Energy's NNSA, under contract 89233218CNA000001.

15

References

- (1) Wolfe, J. P. Thermodynamics of excitons in semiconductors. *Phys. Today* **1982**, *35*, 46–54.
- (2) Clarke, T. M.; Durrant, J. R. Charge photogeneration in organic solar cells. *Chem. Rev.* **2010**, *110*, 6736–6767.
- (3) Tamor, M.; Wolfe, J. Drift and diffusion of free excitons in Si. *Phys. Rev. Lett.* **1980**, 44, 1703.
- (4) Penzo, E.; Loiudice, A.; Barnard, E. S.; Borys, N. J.; Jurow, M. J.; Lorenzon, M.; Rajzbaum, I.; Wong, E. K.; Liu, Y.; Schwartzberg, A. M. et al. Long-range exciton diffusion in two-dimensional assemblies of cesium lead bromide perovskite nanocrystals. ACS nano 2020, 14, 6999–7007.
- (5) Deng, S.; Shi, E.; Yuan, L.; Jin, L.; Dou, L.; Huang, L. Long-range exciton transport and slow annihilation in two-dimensional hybrid perovskites. *Nat. Commun.* **2020**, *11*, 664.
- (6) Giovanni, D.; Righetto, M.; Zhang, Q.; Lim, J. W. M.; Ramesh, S.; Sum, T. C. Origins of the long-range exciton diffusion in perovskite nanocrystal films: photon recycling vs exciton hopping. *Light Sci. Appl.* 2021, 10, 31.
- (7) Yuan, Z.; Zhou, C.; Tian, Y.; Shu, Y.; Messier, J.; Wang, J. C.; Van De Burgt, L. J.; Kountouriotis, K.; Xin, Y.; Holt, E. et al. One-dimensional organic lead halide perovskites with efficient bluish white-light emission. *Nat. Commun.* **2017**, *8*, 14051.
- (8) McClintock, L.; Xiao, R.; Hou, Y.; Gibson, C.; Travaglini, H. C.; Abramovitch, D.; Tan, L. Z.; Senger, R. T.; Fu, Y.; Jin, S. et al. Temperature and Gate Dependence of Carrier Diffusion in Single Crystal Methylammonium Lead Iodide Perovskite Microstructures. J. Phys. Chem. Lett. 2020, 11, 1000–1006.

- (9) Tang, K. W.; Li, S.; Weeden, S.; Song, Z.; McClintock, L.; Xiao, R.; Senger, R. T.; Yu, D. Transport Modeling of Locally Photogenerated Excitons in Halide Perovskites. J. Phys. Chem. Lett. 2021, 12, 3951–3959.
- (10) Chin, X. Y.; Cortecchia, D.; Yin, J.; Bruno, A.; Soci, C. Lead iodide perovskite light-emitting field-effect transistor. *Nat. Commun.* **2015**, *6*, 7383.
- (11) Fu, D.; Zou, J.; Wang, K.; Zhang, R.; Yu, D.; Wu, J. Electrothermal dynamics of semiconductor nanowires under local carrier modulation. *Nano Lett.* 2011, 11, 3809– 3815.
- (12) Graham, R.; Yu, D. Scanning photocurrent microscopy in semiconductor nanostructures. *Mod. Phys. Lett. B* **2013**, *27*, 1330018.
- (13) Wang, X.; Ling, Y.; Chiu, Y.-C.; Du, Y.; Barreda, J. L.; Perez-Orive, F.; Ma, B.; Xiong, P.; Gao, H. Dynamic Electronic Junctions in Organic-Inorganic Hybrid Perovskites. *Nano Lett.* 2017, 17, 4831–4839.
- (14) Xiao, R.; Hou, Y.; Fu, Y.; Peng, X.; Wang, Q.; Gonzalez, E.; Jin, S.; Yu, D. Photocurrent Mapping in Single-Crystal Methylammonium Lead Iodide Perovskite Nanostructures. *Nano Lett.* **2016**, *16*, 7710–7717.
- (15) Fu, Y.; Meng, F.; Rowley, M. B.; Thompson, B. J.; Shearer, M. J.; Ma, D.; Hamers, R. J.; Wright, J. C.; Jin, S. Solution growth of single crystal methylammonium lead halide perovskite nanostructures for optoelectronic and photovoltaic applications. J. Am. Chem. Soc. 2015, 137, 5810–5818.
- (16) Soufiani, A. M.; Huang, F.; Reece, P.; Sheng, R.; Ho-Baillie, A.; Green, M. A. Polaronic exciton binding energy in iodide and bromide organic-inorganic lead halide perovskites. *Appl. Phys. Lett.* **2015**, *107*, 231902.

- (17) Tilchin, J.; Dirin, D. N.; Maikov, G. I.; Sashchiuk, A.; Kovalenko, M. V.; Lifshitz, E. Hydrogen-like Wannier-Mott excitons in single crystal of methylammonium lead bromide perovskite. ACS Nano 2016, 10, 6363-6371.
- (18) Do, T. T. H.; del Águila, A. G.; Cui, C.; Xing, J.; Ning, Z.; Xiong, Q. Optical study on intrinsic exciton states in high-quality CH 3 NH 3 PbBr 3 single crystals. *Phys. Rev. B* **2017**, *96*, 075308.
- (19) Phuong, L. Q.; Nakaike, Y.; Wakamiya, A.; Kanemitsu, Y. Free excitons and exciton—phonon coupling in CH3NH3PbI3 single crystals revealed by photocurrent and photo-luminescence measurements at low temperatures. J. Phys. Chem. Lett. 2016, 7, 4905—4910.
- (20) Ruf, F.; Aygüler, M. F.; Giesbrecht, N.; Rendenbach, B.; Magin, A.; Docampo, P.; Kalt, H.; Hetterich, M. Temperature-dependent studies of exciton binding energy and phase-transition suppression in (Cs, FA, MA) Pb (I, Br) 3 perovskites. APL Mater. 2019, 7, 031113.
- (21) Saba, M.; Quochi, F.; Mura, A.; Bongiovanni, G. Excited state properties of hybrid perovskites. *Acc. Chem. Res.* **2016**, *49*, 166–173.
- (22) Chen, X.; Lu, H.; Yang, Y.; Beard, M. C. Excitonic effects in methylammonium lead halide perovskites. *J. Phys. Chem. Lett.* **2018**, *9*, 2595–2603.
- (23) Wu, B.; Nguyen, H. T.; Ku, Z.; Han, G.; Giovanni, D.; Mathews, N.; Fan, H. J.; Sum, T. C. Discerning the surface and bulk recombination kinetics of organic–inorganic halide perovskite single crystals. *Adv. Energy Mater.* **2016**, *6*, 1600551.
- (24) Baranowski, M.; Plochocka, P. Excitons in metal-halide perovskites. *Adv. Energy Mater.* **2020**, *10*, 1903659.

- (25) Yang, Y.; Yang, M.; Zhu, K.; Johnson, J. C.; Berry, J. J.; Van De Lagemaat, J.; Beard, M. C. Large polarization-dependent exciton optical Stark effect in lead iodide perovskites. *Nat. Commun.* 2016, 7, 12613.
- (26) Hintermayr, V. A.; Polavarapu, L.; Urban, A. S.; Feldmann, J. Accelerated carrier relaxation through reduced coulomb screening in two-dimensional halide perovskite nanoplatelets. *ACS nano* **2018**, *12*, 10151–10158.
- (27) Elbaz, G. A.; Straus, D. B.; Semonin, O. E.; Hull, T. D.; Paley, D. W.; Kim, P.; Owen, J. S.; Kagan, C. R.; Roy, X. Unbalanced hole and electron diffusion in lead bromide perovskites. *Nano Lett.* 2017, 17, 1727–1732.
- (28) Wenger, B.; Nayak, P. K.; Wen, X.; Kesava, S. V.; Noel, N. K.; Snaith, H. J. Consolidation of the optoelectronic properties of CH 3 NH 3 PbBr 3 perovskite single crystals.

 Nat. Commun. 2017, 8, 1–10.
- (29) Yang, Y.; Yang, M.; Li, Z.; Crisp, R.; Zhu, K.; Beard, M. C. Comparison of recombination dynamics in CH3NH3PbBr3 and CH3NH3PbI3 perovskite films: influence of exciton binding energy. *J. Phys. Chem. Lett.* **2015**, *6*, 4688–4692.
- (30) Liu, Y.; Lu, H.; Niu, J.; Zhang, H.; Lou, S.; Gao, C.; Zhan, Y.; Zhang, X.; Jin, Q.; Zheng, L. Temperature-dependent photoluminescence spectra and decay dynamics of MAPbBr3 and MAPbI3 thin films. AIP Adv. 2018, 8, 095108.
- (31) Su, R.; Wang, J.; Zhao, J.; Xing, J.; Zhao, W.; Diederichs, C.; Liew, T. C.; Xiong, Q. Room temperature long-range coherent exciton polariton condensate flow in lead halide perovskites. *Sci. Adv.* **2018**, 4, eaau0244.
- (32) Zhang, S.; Shang, Q.; Du, W.; Shi, J.; Wu, Z.; Mi, Y.; Chen, J.; Liu, F.; Li, Y.; Liu, M. et al. Strong exciton–photon coupling in hybrid inorganic–organic perovskite micro/nanowires. *Adv. Opt. Mater.* **2018**, *6*, 1701032.

- (33) Braun, C. L. Electric field assisted dissociation of charge transfer states as a mechanism of photocarrier production. *J. Chem. Phys.* **1984**, *80*, 4157–4161.
- (34) D'innocenzo, V.; Grancini, G.; Alcocer, M. J.; Kandada, A. R. S.; Stranks, S. D.; Lee, M. M.; Lanzani, G.; Snaith, H. J.; Petrozza, A. Excitons versus free charges in organo-lead tri-halide perovskites. *Nat. Commun.* **2014**, *5*, 3586.
- (35) Fuoss, R.; Accascina, F. Electrolytic conductance; Interscience Publishers, 1959.
- (36) Yamada, Y.; Mino, H.; Kawahara, T.; Oto, K.; Suzuura, H.; Kanemitsu, Y. Polaron Masses in CH₃NH₃PbX₃ Perovskites Determined by Landau Level Spectroscopy in Low Magnetic Fields. Phys. Rev. Lett. 2021, 126, 237401.
- (37) Melissen, S. T. A. G.; Labat, F.; Sautet, P.; Le Bahers, T. Electronic properties of PbX3CH3NH3 (X = Cl, Br, I) compounds for photovoltaic and photocatalytic applications. *Phys. Chem. Chem. Phys.* **2015**, *17*, 2199–2209.
- (38) Senger, R. T.; Bajaj, K. K. Optical properties of confined polaronic excitons in spherical ionic quantum dots. *Phys. Rev. B* **2003**, *68*, 045313.